Planetary and Space Science 57 (2009) 1795–1806

Contents lists available at ScienceDirect

Planetary and Space Science

journal homepage: www.elsevier.com/locate/pss

Detection of dusty plasma near the E-ring of Saturn

J.-E. Wahlund [a,*], M. André [a], A.I.E. Eriksson [a], M. Lundberg [a], M.W. Morooka [a], M. Shafiq [a], T.F. Averkamp [b], D.A. Gurnett [b], G.B. Hospodarsky [b], W.S. Kurth [b], K.S. Jacobsen [c], A. Pedersen [c], W. Farrell [d], S. Ratynskaia [e], N. Piskunov [f]

[a] Swedish Institute of Space Physics, Box 537, SE 751 21, Uppsala, Sweden
[b] Department of Physics and Astronomy, University of Iowa, Iowa City, IA 522 42, USA
[c] Oslo University, Oslo, Norway
[d] NASA/Goddard SFC, Greenbelt MD 20771, USA
[e] Royal Institute of Technology, Stockholm, Sweden
[f] Department for Astronomy and Space Physics, Uppsala University, Uppsala, Sweden

ARTICLE INFO

Article history:
Received 30 November 2008
Received in revised form
26 March 2009
Accepted 30 March 2009
Available online 9 April 2009

Keywords:
Saturn Magnetosphere
E-ring
Cassini
Dust-plasma interaction
Electrodynamic coupling
Plasma physics

ABSTRACT

We present several independent in-situ measurements, which provide evidence that charged dust in the E-ring interacts collectively with the dense surrounding plasma disk of Saturn, i.e., form a system of dust-plasma interaction. The results are based on data sampled by the Radio and Plasma Wave Science (RPWS) investigation onboard Cassini, which allows for interferometry of plasma density inhomogeneities ($\delta n/n$) with two antenna elements and a Langmuir probe sensor. The interferometer experiment detects two ion populations; one co-rotating with the planetary magnetic field and another moving with near Keplerian speed around Saturn. The full range of RPWS measurements indicates that the Keplerian population consists of colder ions ($T_i <$ few eV), which would interact with the electrical potential cavities associated with the few volts negatively charged E-ring water-rich dust grains. The presence of the charged dust inhibits $\mathbf{E}\times\mathbf{B}$ pick-up of freshly ionized particles by the rotating magnetic field of Saturn, since the local potential gradients near the dust grains are stronger than the large-scale co-rotation electric field. Even so, most ions are eventually energised to energies above the dust potentials of a few volts and become part of a hotter co-rotating ion population. The observed results have direct relevance to the interactions occurring in planet forming accretion disks around young stars, since the physical environment is similar.

1. Introduction

The giant planet Saturn and its magnetic field rotate with a period of about 10.7 h, which can be inferred from radio measurements (Gurnett et al., 2004; and references therein). The inner magnetosphere consists of a dense ($<200\,\mathrm{cm}^{-3}$) and cold ($T_e \approx 0.5$–8 eV; $T_i < 100$ eV) plasma in the shape of a disk (e.g., Moncuquet et al., 2005; Persoon et al., 2005; Wahlund et al., 2005; Sittler et al., 2006; Gustafsson and Wahlund, 2009), which extends to a denser equatorial region in the outer magnetosphere (Morooka et al., 2009). Plasma in this magnetosphere is mostly "frozen into" the magnetic field and therefore tends to be picked-up and co-rotate with this field (and the planet) by the action of an induced co-rotation electric field ($\mathbf{E}_{rot} = -\mathbf{v}_{rot}\times\mathbf{B}$). The rotation speed of the plasma therefore increases with the distance from Saturn (tending to approach $\mathbf{v}_{rot} = \boldsymbol{\Omega}\times\mathbf{r}$), as indeed can be observed by the CAPS ion spectrometer (e.g., Young et al., 2005; Sittler et al., 2006). Therefore, it was a surprise that RPWS Langmuir probe (LP) results indicated ion drift speeds significantly lower than co-rotation in the inner ($<6\ R_S$, Saturn radii) near equatorial magnetosphere (Wahlund et al., 2005), and seemed to contradict the CAPS results. Modulations of the rotation period of Saturn's plasma disk (Gurnett et al., 2007) and the outer magnetospheric plasma (Morooka et al., 2009) are also clearly detected, suggesting that a yet unknown process cause a longitudinal asymmetry and an outflow of plasma from the inner plasma disk. This modulation process could in principle be generated by a two-cell convection pattern (Dessler et al., 1981; Hill et al., 1974), coupled with centrifugally driven outflows (Hill and Michel, 1976).

Compared to co-rotation, larger debris is instead mostly affected by the gravitational field of Saturn, and consequently tend to follow Keplerian orbits around the planet. The speed of this debris therefore decreases with distance from Saturn ($v = \sqrt{GM/r}$). The gravitation and the co-rotation forces acting on such charged particles clearly compete depending on mass,

* Corresponding author. Tel.: +46 18 4715946; fax: +46 18 4715905.
E-mail address: jwe@irfu.se (J.-E. Wahlund).

0032-0633/$ - see front matter © 2009 Elsevier Ltd. All rights reserved.
doi:10.1016/j.pss.2009.03.011

charge, electric and magnetic field magnitudes. For the charged nanometer- and micrometer-sized dust in the E-ring, both forces may be important as shown by in-situ observations here, and for the dynamics of stream particles from the E-ring (e.g., Horányi, 2000).

The distribution of dust has been measured in the E-ring by several investigations (e.g., Kurth et al., 2006; Srama et al., 2006; Kempf et al., 2008; and references therein), and the E-ring has been found to extend from 3 to 8 R_S near the equatorial plane and to encompass several icy moons. Theoretical modelling suggests the E-ring expands even beyond 8 R_S (Horányi et al., 2008), and the Cassini dust experiment (CDA) indicates the rings extent reaches Titan's orbit (Srama et al., 2006). Based on data from grain sizes $>1\,\mu m$, it has been concluded that Enceladus feeds a dust torus that disperses to form most of the E-ring. Dust densities of these larger grains are $\sim 0.1\,m^{-3}$ ($10^{-7}\,cm^{-3}$), which is small compared to plasma densities in the surrounding plasma disk. However, the dust population follows a $r_d^{-\mu}$ power law ($\mu \approx 4$–5) (Kempf et al., 2008), where r_d is the dust grain radius, and dust densities therefore rise sharply for smaller dust particles and the E-ring is by far dominated by sub-μm-sized grains. Stream particles of nm-sized grains (e.g., Kempf et al., 2005) were detected during the spacecraft approach to Saturn in interplanetary space. These so-called Saturnian stream particles mostly originate from the E-ring. Recent electron spectrometer (CAPS/ELS) measurements also indicate that large amounts of nm-sized grains are ejected from the southern hemisphere exhaust plumes on Enceladus (Jones et al., 2008), which agrees well with models of the plume dust distribution (Scmidt et al., 2008).

The charge of the dust in the E-ring has been measured by the dust experiment (CDA) (Kempf et al., 2006) to be a few volts negative inside 7 R_S (and positive outside the orbit of Rhea). These potentials correspond rather well with measured Cassini spacecraft potentials in the plasma disk (Wahlund et al., 2005; Sittler et al., 2006; and shown here). The spacecraft potential of Cassini can therefore be used as a reasonable proxy for the grain charging, even considering the difference in chemical properties between water ice grains and the spacecraft, and their different sizes with respect to the Debye length (c.f., Section 4).

The dense inner plasma disk surrounding the E-ring can interact with the charged dust grains near the equatorial plane through electromagnetic forces as a collective dusty plasma ensemble where the dynamics are significantly different from the case when considering the particle populations separately (e.g., Goertz, 1989; Northrop, 1992; Horányi et al., 2004). Such ensembles have been observed in the laboratory (e.g., Morfill et al., 2002) and in the upper atmosphere of Earth (e.g., Havnes et al., 1996), and are inferred to exist in several space, proto-planetary and astrophysical environments (e.g., Alfvén, 1984). Electrostatic coupling of micron-sized dust has also been inferred in the more visible inner rings of Saturn in the form of "spokes" (Smith et al., 1981, 1982; Hill and Mendis, 1982; Goertz et al., 1986). The conditions in the plasma disk near the equatorial plane are such that $r_d \ll d_g \ll \lambda_D$, where r_d, d_g and λ_D are the typical grain radius, the inter-grain distance and the plasma Debye length, respectively. In the case where $d_g < \lambda_D$, the charged dust participates in the screening process and therefore in the collective behaviour of the ensemble. In the case where $\lambda_D < d_g$, the dusty plasma can be considered as a collection of isolated screened grains.

In this paper we present data from the Radio and Plasma Wave Science (RPWS) instruments onboard the Cassini spacecraft when traversing the inner plasma disk of Saturn, which accurately determines the plasma conditions and the spacecraft potential, and detects two types of ion-timescale inhomogeneities in the plasma with a plasma density ($\delta n/n$) interferometer. In addition, a clear difference in electron and ion densities can be detected during ring plane crossings near Enceladus, which indicates significant electron attachment to dust particles (see also Farrell et al., 2009). Derived dust distributions are consistent with the measured difference (Yaroshenko et al., 2009). Furthermore, the detection of two ion populations with different drift speeds can explain the apparent inconsistency between CAPS and RPWS LP ion drift measurements (Wahlund et al., 2005; Jacobsen et al., 2009).

The paper is organized as follows. In Section 2 the RPWS measurement techniques used are described. In Section 3 the $\delta n/n$ interferometer results are presented from two flybys of the plasma disk. In Section 4 the plasma conditions for the two flybys are presented using the LP and plasma wave data. In Section 5 the LP and plasma wave data from an Enceladus pass is presented. Discussion and conclusions are presented in Sections 6 and 7, respectively.

2. RPWS experiment methods

2.1. Electron number density from upper hybrid emissions

A full description of the RPWS instruments can be found in Gurnett et al. (2004). The RPWS investigation employs several different methods to estimate the electron number density (n_e). One method makes use of the upper hybrid emission line which peaks in electric spectra at the frequency $f_{UH} = \sqrt{f_{ge}^2 + f_{pe}^2}$, where f_{ge} is the electron gyro-frequency and f_{pe} is the electron plasma frequency. Knowing the magnetic field strength gives n_e. For most of the measurements in the inner plasma disk of Saturn, $f_{ge}^2 \ll f_{pe}^2$. Another method makes use of LP voltage sweeps as described below.

2.2. Langmuir probe (LP) voltage sweeps

The spherical 5 cm diameter LP sensor is situated 1.5 m from the Cassini spacecraft main body. It samples the total electrical current from the plasma by making 512 points voltage sweeps (± 32 V) usually every 10 min (each 24 s during targeted flybys). This method gives estimates of several thermal plasma parameters of importance for characterizing the properties of the inner magnetosphere of Saturn (Wahlund et al., 2005), of which the electron and ion number densities (n_e and n_i), electron temperature (T_e) and ion drift speed (v_i) are relevant for this study. The voltage sweep also gives estimates of the spacecraft potential (U_{SC}), which is calculated from the spacecraft potential measured at the probe (U_1 or floating potential) according to $(U_{SC} - U_1) = c \cdot \exp(-d_{LP}/\lambda_D)$, where $d_{LP} = 1.5$ m is the distance of the probe to the spacecraft main body surface, λ_D the Debye length of the surrounding plasma and $c \approx 5/6$ is a constant.

The electron parameter results are based on a three-electron component theoretical fit to the LP voltage sweeps (e.g., Mott-Smith and Langmuir, 1926; Medicus, 1962; Whipple, 1965; Hoegy and Brace, 1999). One electron component corresponds to the spacecraft photoelectrons (of no interest here), while the others give the values of the core magnetospheric electron populations. It is therefore most often possible to correct for the photoelectron contamination from the spacecraft. The electron current to the probe in Orbit Motion Limited (OML) approximation for one electron population, for positive voltages, can be written as

$$I_e = I_{e0}(1 - \chi_e)$$

where

$$I_{e0} = A_{LP} n_e q_e \sqrt{\frac{k_B T_e}{2\pi m_e}}$$

is the random current, A_{LP} is the probe area, and

$$\chi_e = \frac{q_e(U_{bias} + U_1)}{k_B T_e}$$

where U_{bias} is the applied bias voltage and U_1 is the floating potential (in case of spacecraft photoelectrons), or the characteristic potential of the electron population in the plasma (in case of ambient plasma electrons). For negative voltages, $(U_{bias}+U_1)<0$ the electron temperature is estimated from the exponential part as

$$I_e = I_{e0} \exp(-\chi_e)$$

Fig. 1 shows an example of a voltage sweep from orbit 26 with a superimposed theoretical fit (red line). Here the same data is represented in linear (panel a), logarithmic (panel b) and the derivative (dI/dU, panel c).

The negative voltage part gives information on ion drift speed (e.g., Fahleson et al., 1974), ion number density, average ion mass and integrated solar EUV intensity (photoelectrons emitted from the probe). The ion contribution to the current is given by

$$I_i = I_{i0}(1 - \chi_i)$$

where the random current

$$I_{i0} \approx -A_{LP} n_i q_i \frac{|v_i|}{4}$$

and

$$\chi_i \approx \frac{q_i(U_{bias} + U_1)}{m_i v_i^2/2e}$$

are assumed to be dominated by the ion ram flux to the probe. A possible finite thermal component ($k_B T_i$) in the inner magnetospheric plasma will have the effect of decreasing the derived ion drift speed in the analysis, since it gives an additional current contribution. The photoelectron current emitted from the probe is a constant for negative voltages ($I_{ph,0}$) and is, like the ion current, exponentially decreasing for positive voltages $(U_{bias}+U_1) > 0$ as (Grard, 1973)

$$I_{ph} = I_{ph,0}\left(1 + \frac{e(U_{bias} + U_1)}{k_B T_{ph}}\right) \exp\left(-\frac{e(U_{bias} + U_1)}{k_B T_{ph}}\right)$$

Error ranges depend on sweep signal strength and type of parameter estimated. The electron number density and spacecraft floating potential estimates have inherent errors below 10% in the plasma disk regions presented here. Systematic errors of the electron number density may be larger since it is difficult to identify a possible hot (>10 eV) electron component in the sweeps. Furthermore, the possible effects of current contributions from impacts of energetic radiation belt particles and associated secondary electrons (Eriksson and Wahlund, 2006) are not included in the analysis, as such anomalously enhanced probe currents have so far only been detected in the region 6–15 R_S.

2.3. $\delta n/n$ interferometer

The RPWS experiment facilitates interferometry of plasma density inhomogeneities ($\delta n/n$) with the use of two 10 m antenna elements (denoted "Eneg" and "Epos") and the spherical LP sensor, by sampling the waveform of the electric current from these sensors. For this purpose we make use of a three channel-WFR (waveform) receiver that is sampling at 7000 samples/s. The speed of inhomogeneities in the plasma for different scale sizes (frequencies) can be estimated by measuring the time difference (phase) for $\delta n/n$ signals to travel between the three displaced sensors. The observed phase of a wave signal with wave vector **k**

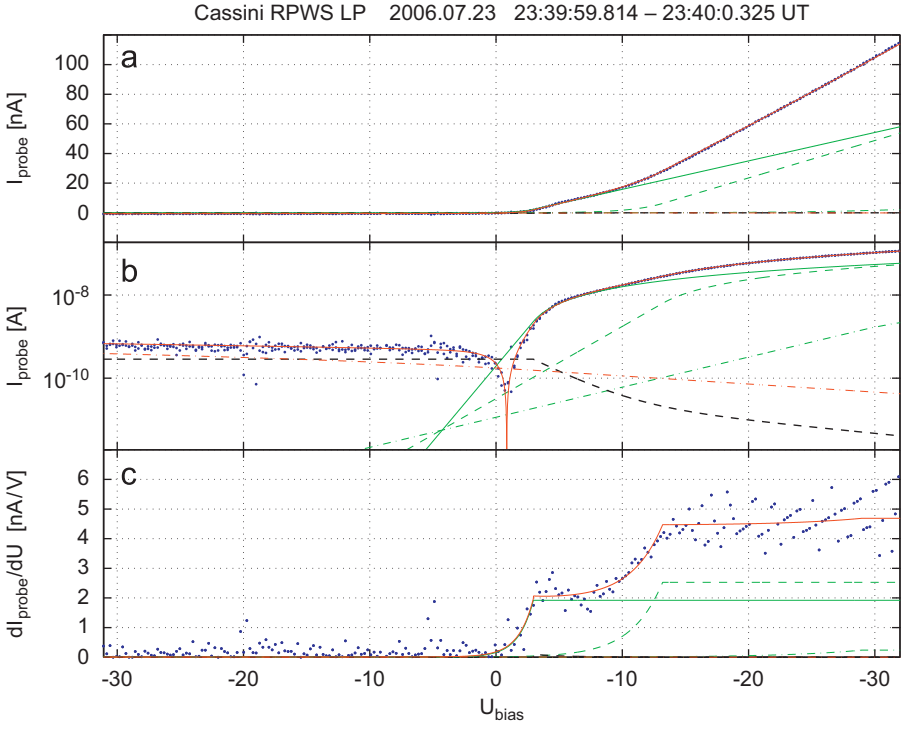

Fig. 1. Current-voltage characteristics of a bias voltage sweep from Rev26. The same data are displayed in linear (panel a), absolute logarithmic (panel b) and the derivative (panel c). Three electron populations (green lines) were used in this particular fit. The ion current (red, dashed-dot) and photoelectron current from the probe (black dashed) is added to the total theoretical current (red line), which fits the RPWS LP data (blue dots) very well.

can generally be written as

$$\varphi = \mathbf{k}\cdot\mathbf{d} + n\pi$$

where the distance vector between two $\delta n/n$ sensors is **d**. The phase dispersion is then

$$\frac{\partial\varphi}{\partial\omega} = \frac{\partial}{\partial\omega}[\mathbf{k}\cdot\mathbf{d} + n\pi] \Rightarrow \frac{\partial\omega}{\partial k} = (\hat{k}\cdot\hat{d})d\left[\frac{\partial\varphi}{\partial\omega}\right]^{-1}$$

The signal will be Doppler shifted according to

$$\omega = \omega_0 + \mathbf{k}\cdot\mathbf{v}_s$$

where ω_0 is the rest frequency and $\mathbf{v}_s = (\mathbf{v}_{SC}\text{-}\mathbf{v}_{plasma})$ is the relative velocity vector between the spacecraft and the plasma. This gives another expression for the frequency dispersion

$$\frac{\partial\omega}{\partial k} = \frac{\partial\omega_0}{\partial k} + (\hat{k}\cdot\hat{v}_s)v_s$$

Equating these two expressions for the frequency dispersion gives the general equation for $\delta n/n$ interferometry between two sensors

$$\frac{\partial\omega_0}{\partial k} + (\hat{k}\cdot\hat{v}_s)v_s = (\hat{k}\cdot\hat{d})d\left[\frac{\partial\varphi}{\partial\omega}\right]^{-1}$$

Here the first term on the left-hand side is the group velocity of plasma waves (= 0 for plasma irregularities), and the second term becomes v_s for spatial plasma inhomogeneities. Knowing the geometry of the problem (the angle, θ_{sd}, between the relative spacecraft velocity vector and the distance vector between the probes) therefore gives a possibility to estimate the speed of the plasma density inhomogeneities as

$$v_s = \cos\theta_{sd}\, d\left(\frac{2\pi\Delta f}{\Delta\varphi[rad]}\right)$$

from a phase-frequency relationship, where the frequency gives the scale size of the plasma inhomogeneities in question. This method has been used successfully on several spacecraft missions around Earth (e.g., Kelley and Mozer, 1972; Temerin, 1978; Holmgren and Kintner, 1990; Bonnell et al., 1996; Wahlund et al., 1998), and on Cassini it has so far been carried out a few times in the plasma disk and near Titan.

3. Interferometer and WFR results

We present here two short periods of RPWS interferometer experiments carried out in the plasma disk during orbits 17 and 26. Both occurred just outside the orbit of Enceladus ($\approx 4\ R_S$) at distances between 4.2 and 5.0 R_S, and near the Kronian equatorial plane (0.2–0.3° LAT and 3.6–9.6° LAT, respectively). During the chosen time intervals, the spacecraft was oriented so that the two long RPWS antenna and the LP were aligned in the ideal co-rotation ram direction (Fig. 2).

For the interferometer event during orbit 17 (Figs. 3–5) one can identify a coherent broadband signal below approximately 400 Hz, where the power spectral density peaks at the lowest measured frequencies (Fig. 3, panels a and b). There is also a signal around 1 kHz, which is identified as electromagnetic Chorus emissions. Note that the measurements with long 10 m antenna depend on the 1/RC coupling to the plasma (Eriksson and Boström, 1995; Kellog et al., 2009), and for this case sampling below 500 Hz pertains to a $\delta n/n$ response, while above 500 Hz the long antenna instead samples the electric field (δE) component. This is confirmed by the behaviour of the phase response above this frequency for the two long antenna interferometer component (Fig. 4, panel a), where the Chorus emissions attain the expected antenna phase difference of 120° in the frequency interval 700–1600 Hz in accordance with the long antenna geometry. Furthermore, the small 5 cm diameter LP detects only the low frequency broadband emissions, as it is only affected by a $\delta n/n$ signal in this plasma environment and therefore do not

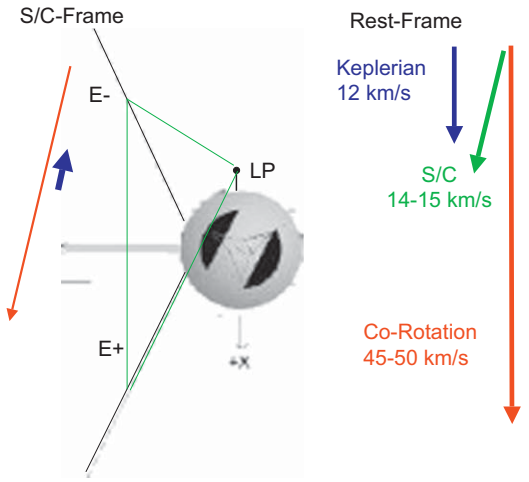

Fig. 2. Experimental setup during the two presented $\delta n/n$ interferometer runs on Rev17 and Rev26 presented here. The ideal co-rotation and gravitational speeds are noted. The spacecraft attitude was selected so that the two 10 m long RPWS antenna (Eneg & Epos) and the Langmuir probe (LP) was in co-rotation ram. Note that the Keplerian speed in the S/C frame of reference is small and may be opposite the co-rotation flow.

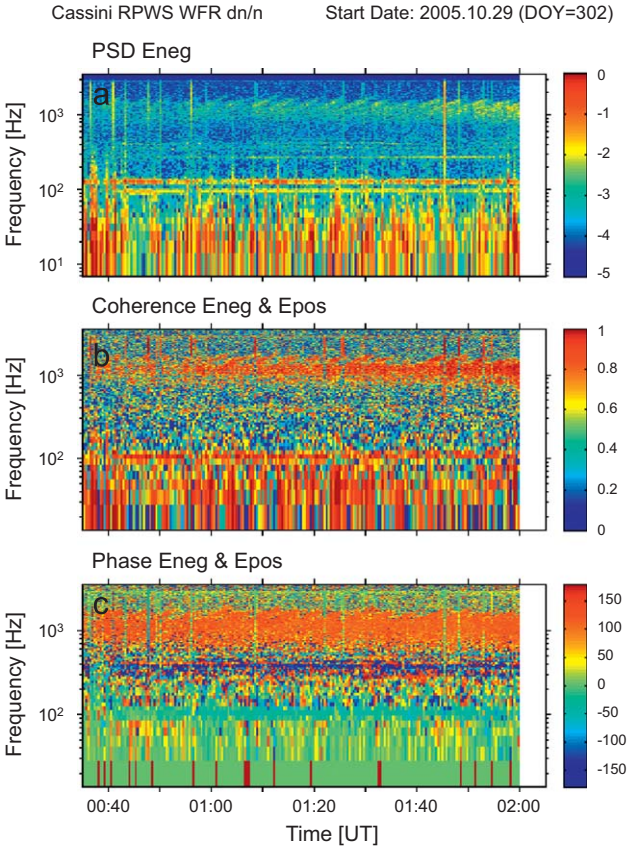

Fig. 3. Power spectral density (PSD) of the long Eneg RPWS antenna (panel a) during the $\delta n/n$ interferometer run on Rev17, together with the coherence (panel b) and phase (panel c) between the Eneg and Epos antenna. A coherent broadband signal can be detected below about 400 Hz. A Chorus can also be detected near 1 kHz.

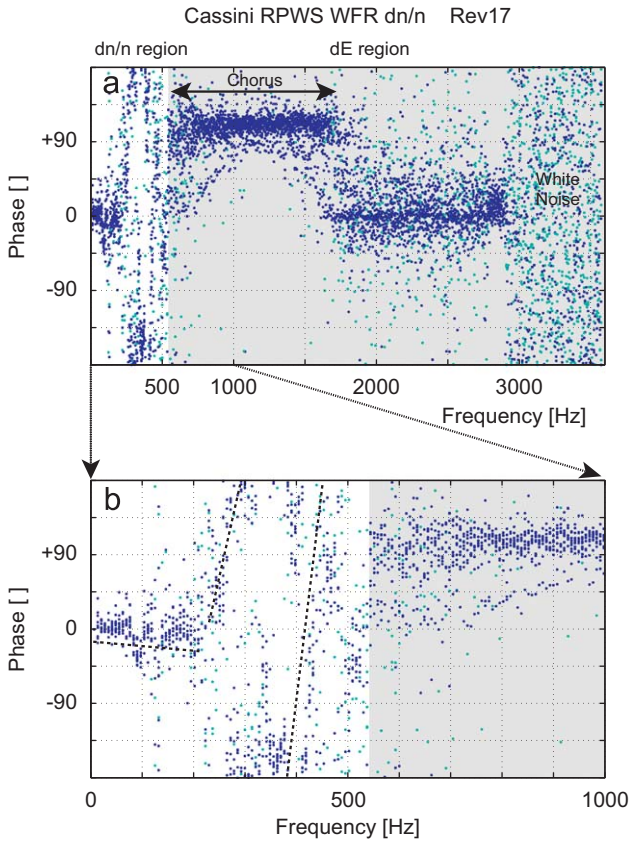

Fig. 4. Phase during the whole interferometer run on Rev17. The phase was constructed by averaging 16 ffts of 1024 points each. The 13 resulting averages are superposed here. Points with coherence below 0.05 are shown in cyan. Panel a show all data, while panel b focus on the $\delta n/n$ region below 500 Hz (non-shaded). Two distinct ion population inhomogeneities corresponding to co-rotation and Keplerian speeds can be identified. Guiding lines (black dashed) have been added. See text for further description.

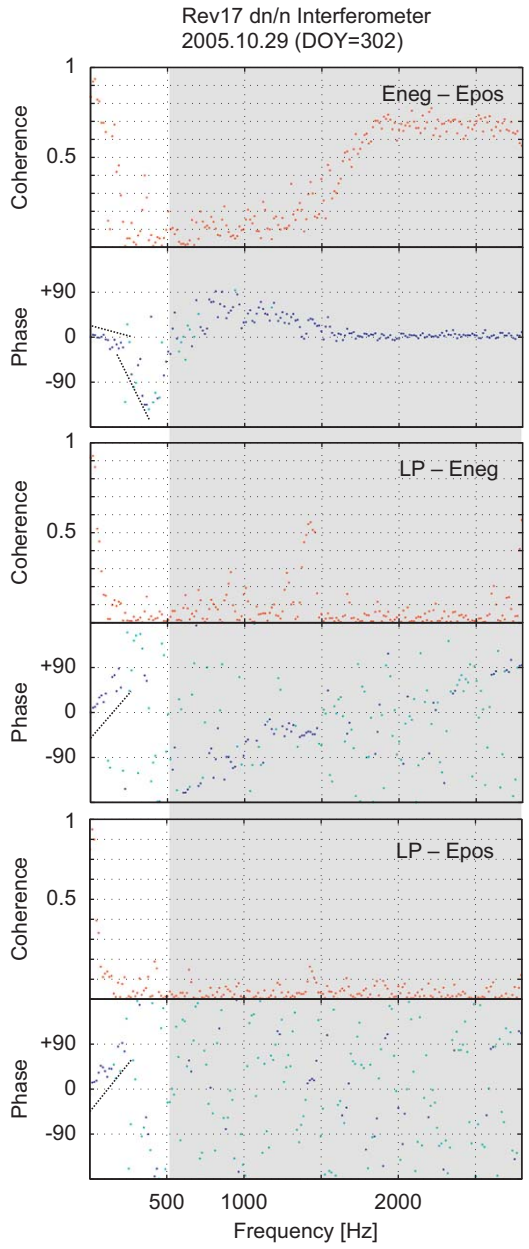

Fig. 5. Coherence and phase for each sensor-pair during the first 5 min of the $\delta n/n$ interferometer run during Rev17. A clear slope can be identified in all sensor-pair combinations that correspond to a slow Keplerian speed of inhomogeneities in the plasma. Guiding lines (black dashed) have been added.

detect the Chorus emissions (not shown). There is also a low-pass filter applied to the sampling (Fig. 4, panel a), and expectedly there is only incoherent white noise detected above about 2800 Hz.

The phase displayed in Fig. 4 is constructed by making 1024 points Hanning windowed Fourier transforms, and doing an average of 16 such transforms, thus gaining 13 such averages for the period of interferometry (October 30, 2005, 00:30–02:00 UT). It is clear from Fig. 4 (panel b) that two frequency intervals with different $d\varphi/df$ characteristics exist. One below 200 Hz has an average of $d\varphi/df \approx 75^\circ$/kHz for $d = 8.7$ m, but can be allowed to vary between 0.0022° and 0.112°/Hz according to the data uncertainty. This phase response corresponds to speeds of inhomogeneities relative to the spacecraft between 28 and 140 km/s $\times \cos\theta_{sd}$, with an average of 42 km/s $\times \cos\theta_{sd}$, and is therefore consistent with a co-rotating plasma of about 35 km/s relative to the spacecraft, since $\theta_{sd} \approx 0$.

The second frequency interval between 200 and 500 Hz is characterised by much steeper gradients, $d\varphi/df \approx 2.0$–4.0°/Hz, which correspond to speeds relative to the spacecraft of 0.8–1.6 km/s $\times \cos\theta_{sd}$. The measured speed of these slower inhomogeneities in the plasma is in the opposite direction compared to the co-rotating flow as measured in the spacecraft frame of reference. However, this is an average result and when studying the phase response for shorter time periods, this slower population varies between ± 6 km/s $\times \cos\theta_{sd}$ and around 0, and depends strongly on frequency (scale size). The slower population is consistent with a near Keplerian motion around Saturn, which is close to the spacecraft azimuthal speed component.

In Fig. 5 the coherence and phase of each sensor-pair are presented for the first part of the interferometer period during orbit 17. These data are Hanning windowed 512 points Fourier transforms, 50% overlap and 36 averages. The coherence is often below 0.1 above 300 Hz in the $\delta n/n$ region (below 500 Hz). Even so, it is clear that a slow component exists between the three possible sensor pairs with inferred speeds between 3 and 6 km/s. The interferometry between the LP and the long Epos antenna is most often completely incoherent, and this may be due to the fact that these sensors are situated on the opposite side of the spacecraft and that the moving inhomogeneities possibly become disturbed by the spacecraft. This is the case if the slower inhomogeneities are associated with heavy dust grains that ram

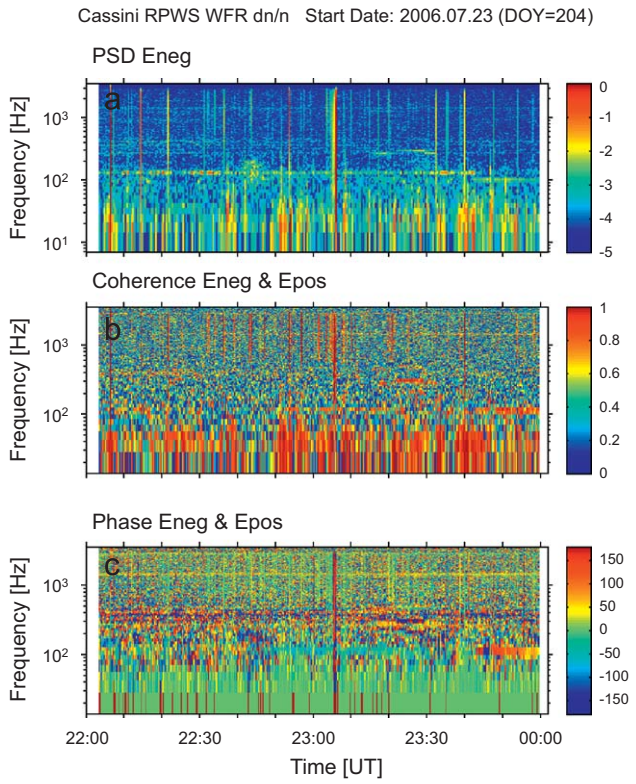

Fig. 6. Power spectral density (PSD) of the long Eneg RPWS antenna (panel a) during the $\delta n/n$ interferometer run on Rev26, together with the coherence (panel b) and phase (panel c) between the Eneg and Epos antenna. A coherent broadband signal can be detected below about 400 Hz.

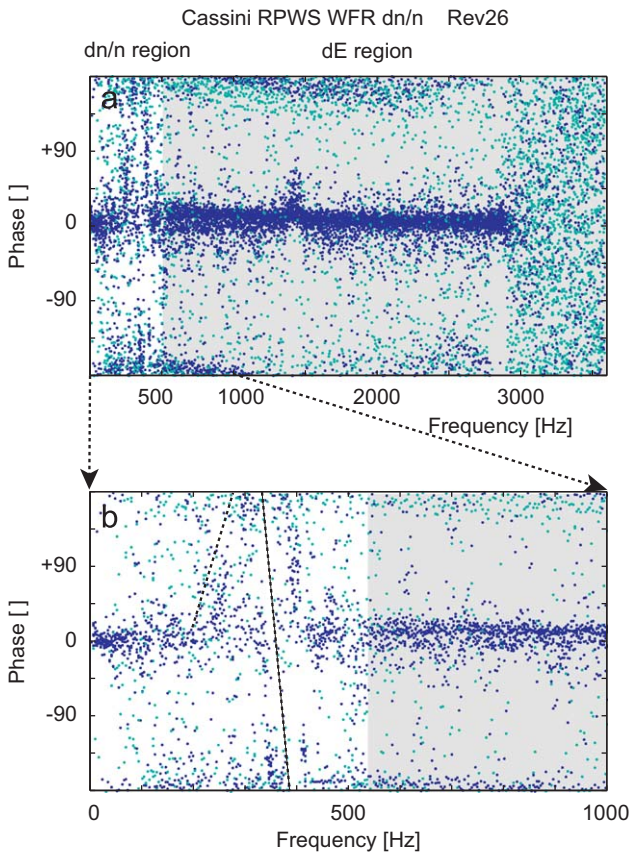

Fig. 7. Phase during the whole interferometer run on Rev26. Same type of plot as in Fig. 4. Inhomogeneities corresponding to near Keplerian speeds can be identified. Guiding lines (black dashed) have been added. See text for further description.

the spacecraft and therefore disappear before hitting the second sensor.

The WFR interferometer measurements for the event during orbit 26 (Figs. 6 and 7) show similar characteristics as the event during orbit 17, but the signal is weaker and no Chorus emissions appear. Again there exists a coherent low frequency broadband signal below a few 100 Hz (Fig. 6, panels a and b). The phase response (Fig. 7, panel b) of the $\delta n/n$ signal below 500 Hz again shows two different characteristics. The speed for the faster component (<200 Hz) can in this case not be resolved, and has to be larger than a minimum estimate of 35 km/s $\times \cos\theta_{sd}$, while the slower component is fluctuating on the average around 0 ± 1.5 km/s $\times \cos\theta_{sd}$.

4. Langmuir probe thermal plasma results

The RPWS derived thermal plasma parameters during the interferometer events described above are presented in Figs. 8 (orbit 17) and 9 (orbit 26). Calibrated raw sweep data are displayed in panel a, where electron sampling occurs for positive bias potentials and ion sampling or photoelectron emission from the probe occurs for negative bias potentials. The electron number density (panel b) is derived either from the upper hybrid emissions (black line) or the LP sweeps (blue dots) and is 60–70 cm^{-3} during the event on orbit 17, and significantly lower, 15–40 cm^{-3}, during the event on orbit 26, which explains the lower interferometry signal strength on orbit 26. The electron temperatures (panel c, cyan) are estimated to be 4 eV (orbit 17) and 2–5 eV (orbit 26). Note, though, that it is possible to identify a hotter electron component (green stars) at times, and this could be due to an anisotropic electron population with a temperature ratio of 2–2.5 (see also Gustafsson and Wahlund, 2009).

Unfortunately, the spherical LP cannot differ between temperature characteristics perpendicular and parallel to the magnetic field. The corresponding Debye lengths during the interferometer events are therefore $\lambda_D \approx 1.8$–1.9 m (orbit 17) and 1.7–4.3 m (orbit 26), and if a temperature anisotropy exists these values shall be increased by a factor 1.2–1.3. The Debye lengths during the two events are therefore in the range 2–5 m.

The spacecraft potential (blue) is shown in panel d in Figs. 8 and 9, and its estimation is based on the lower electron temperature in panel c. The spacecraft potential is -6 to -8 V (orbit 17) and -10 to -4 V (orbit 26). Dust grains in this region should be charged to similar potentials, and even though they consist of significantly different materials, they are exposed to the same charging mechanisms as the Cassini spacecraft. As the Debye length is not much smaller than the spacecraft dimensions, the magnitude of the spacecraft potential should only be slightly larger than the dust potential magnitude. The charge of the dust in the E-ring has also been measured by the dust experiment (CDA) (Kempf et al., 2006) to be a few volts negative during Saturn orbit injection (orbit 0), supporting the procedure of using the U_{SC} as an approximate proxy for dust grain charge. The charging of grains larger than about 100 nm is size independent (e.g., Horányi, 1996), and variations of grain potential is either due to grain material (unlikely since most E-ring grains consist of water ice), or due to fluctuations in plasma properties (assuming charge equilibrium). The number of excess electrons on a >100 nm grain is about 700 V^{-1} (see e.g., Horányi et al., 2004). For smaller dust particles, the charging is size dependent. The average charge on each dust grain can be approximated by $700e \times r_d[\mu m] \times U_{SC} \approx 200$–$7000$ eC during the interferometry events.

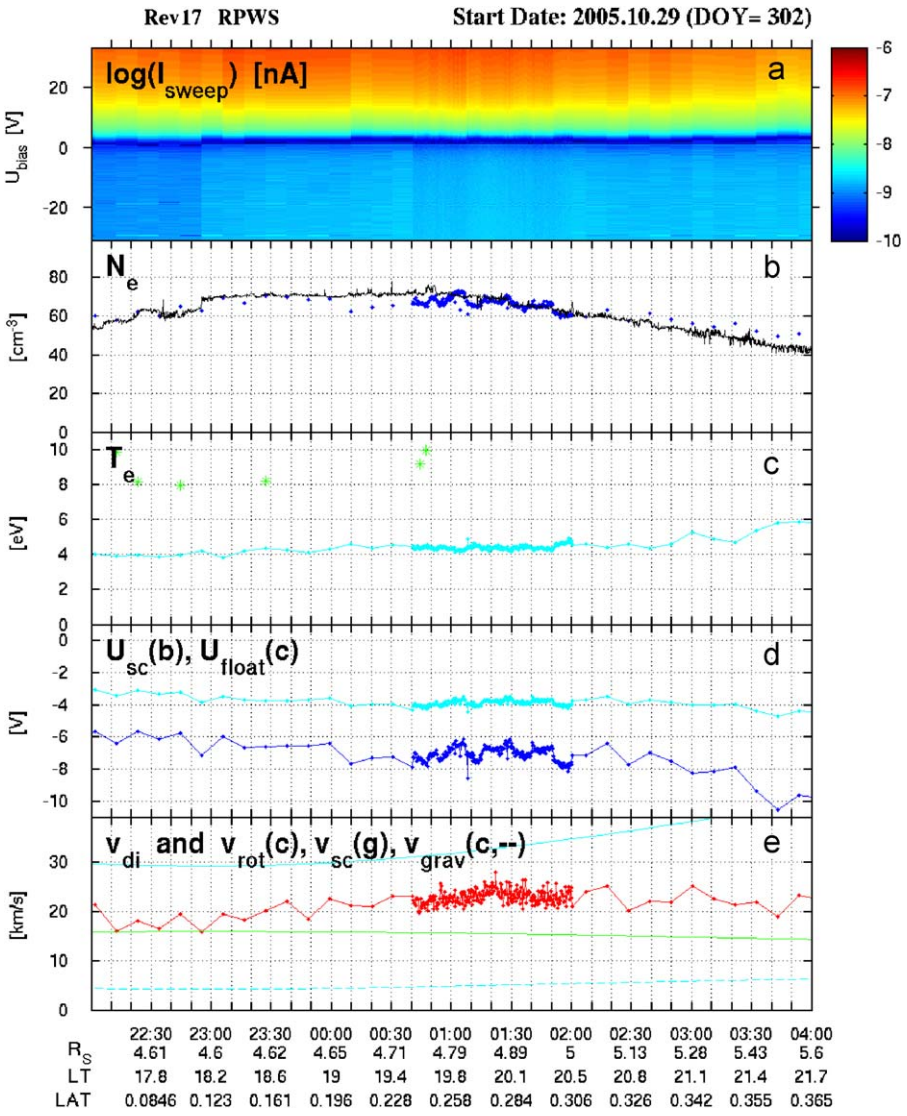

Fig. 8. Summary plot of the Langmuir probe data around the $\delta n/n$ interferometer event during Rev17, 00:30–02:00 UT. Raw sweep data (panel a) showing the electron sampling (positive bias) and ion sampling (negative bias), and the electron density (panel b) derived from LP (blue dots) and Fuh emissions (black line) agree. An occasional hotter electron component (green stars, panel c) can be identified. The ion drift speed (red, panel e) falls between the co-rotation (cyan) and Keplerian (cyan dashed) speeds in the spacecraft reference frame. The spacecraft speed in the rest frame (green) is shown for comparison.

The average ion drift speed (panel e, Figs. 8 and 9) can be estimated in two ways from LP voltage sweeps. A parametric fit to the sweep data estimates the random ion current ($I_{i0} \propto n_i v_i$) and the gradient at negative voltages ((*dI*/*dU*). The ratio

$$W_i = I_{i0}/(dI/dU) \approx m_i v_i/2e[\mathrm{eV}]$$

is the ion energy, and by assuming water group ions (18 amu) one can derive the ion drift speed (v_i, red in panel e). The other method makes use of the fact that the random ion current is directly proportional to the ion ram flux ($I_{i0} \propto n_i v_i$), and by assuming $n_i = n_e$, gives the ion drift speed (black dots). The first method is more accurate measurement-wise and does not include errors from the electron component. It is also less sensitive to errors induced by secondary electrons from energetic particle or dust impacts, since it depends on $\sqrt{I_{i0}}$ (from equation above). During the orbit 17 event, there are significantly enhanced currents for negative voltages (not shown), which are most probably due to substantial dust impacts on the LP sensor. The displayed ion drift speeds are therefore overestimated for the orbit 17 event. The average ion drift speeds are significantly lower than the co-rotational speed relative to the spacecraft (cyan line) in both events, but stay above the Keplerian speeds (dashed cyan).

To illustrate the consistency between the ion and electron data during the orbit 26 event, we included the ion density derived from the ion random current (ion flux), assuming the spacecraft speed (green dots, panel b in Fig. 9). Only a small deviation (of unknown nature) can be seen near 23:30 UT. The small LP derived electron density mismatch near 22:20 UT is due to a photoelectron contribution from the spacecraft that was difficult to compensate for. The agreement with upper hybrid derived densities is otherwise very good.

5. The E-ring plane crossing during the Enceladus E02 encounter

Fig. 10 displays the RPWS thermal plasma characteristics during the E02 Enceladus encounter on July 14, 2005. Here the sweep analysis clearly identifies two electron temperatures (panel c) with $T_{e1}/T_{e2} \approx 2.0$–2.5, and $T_e \approx 1.5$–5.5 eV. These are either due to a electron temperature anisotropy parallel and

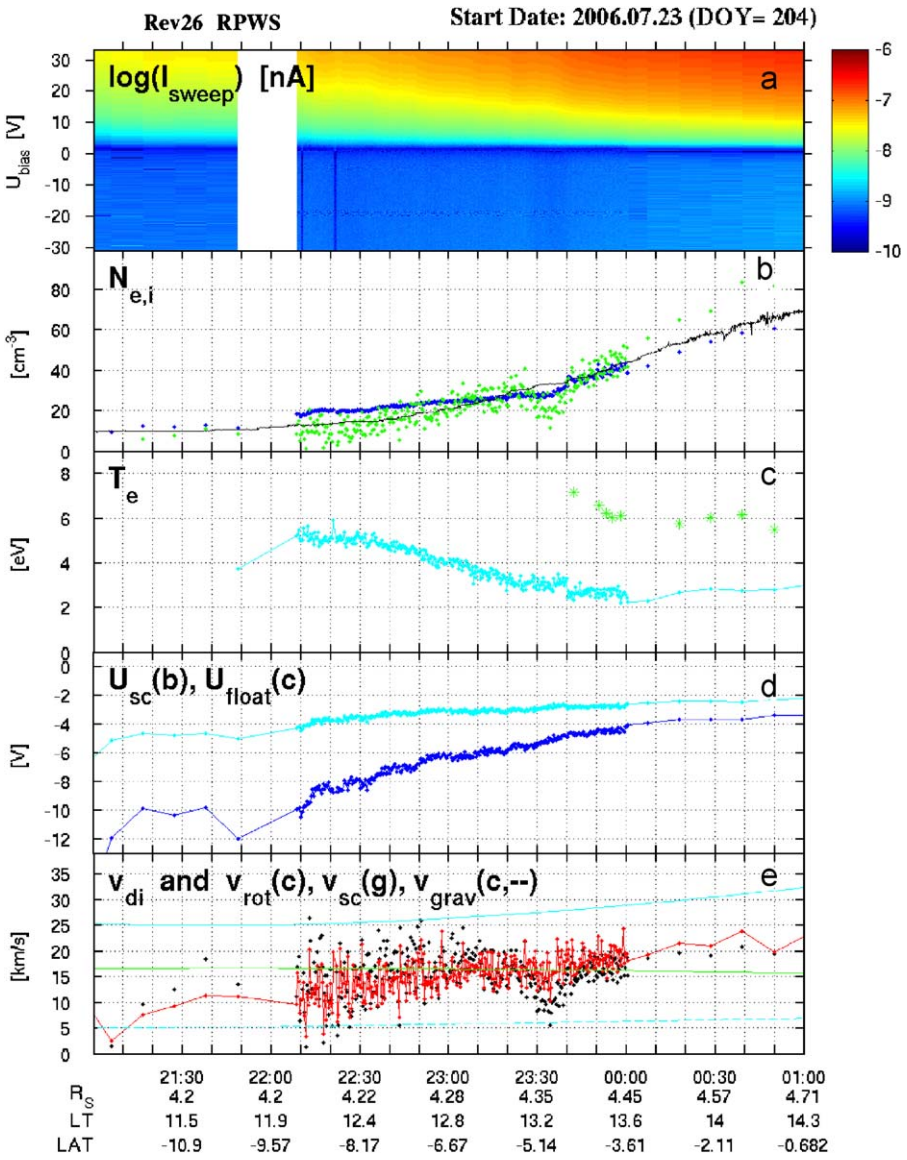

Fig. 9. Same as in Fig. 8. Summary plot of the Langmuir probe data around the $\delta n/n$ interferometer event during Rev26, 22:10–00:00 UT. See text for further description. The green dots in panel b are the estimated ion density assuming the ions hit the probe with the spacecraft speed. The black dots in panel e correspond to a drift speed estimated solely from the dc-level (random current) of the sweep voltage-current characteristics, and agree well with the gradient derived average ion drift speed (red dots, panel e). See text for further description.

perpendicular to the Kronian magnetic field, or possibly from two different electron populations. There is a distinct decrease in the electron temperature at the ring plane crossing just before closest approach (C/A) of Enceladus at 19:52:30 UT. The electron density derived from the upper hybrid emissions (black line, panel b, and Fig. 11) are difficult to account for during the period near closest approach due to the large amounts of E-ring dust impacts on the electric antenna sensors. These dust impacts are detected as a broadband noise up to large frequencies roughly between 19:33 and 20:10 UT and is very pronounced near the E-ring plane crossing at 19:53 UT (Fig. 11) (see also e.g., Kurth et al., 2006). The electron densities derived from LP voltage sweeps (blue dots in Fig. 10) give a better account here, and a clear decrease in n_e to $\approx$30–40 cm^{-3} can be detected near the ring plane crossing, while the surrounding electron densities are 60–70 cm^{-3}. The continuous 20 Hz density data, i.e., the electron current sampled at a constant bias voltage of +10 V, is added in panel b, Fig. 10 (cyan). The sampled 20 Hz current is proportional to

$$n_e\sqrt{T_e}\left(1+\frac{1}{T_e}(U_{SC}+U_{bias})\right)$$

and can therefore also be affected by the electron temperature and spacecraft potential, which is the reason why a perfect one-to-one relationship to the sweep derived electron density is not seen in Fig. 10, panel b. Nevertheless, it enforces the fact that the electron density decreases by a factor 2 near the ring plane crossing. Debye lengths vary between 1.0 and 1.5 m during the event. The spacecraft potential varies between −2 and −3 V (panel d, Fig. 10), and the average ion drift speeds derived from LP sweeps (red and black in panel e, Fig. 10) are significantly lower than the Saturn co-rotation speed in the spacecraft reference system (cyan).

It is informative to compare with the ion density (n_i, red dots in panel b, Fig. 10) derived from the ion random current (ion ram flux) and using the derived ion drift speed in panel e. During

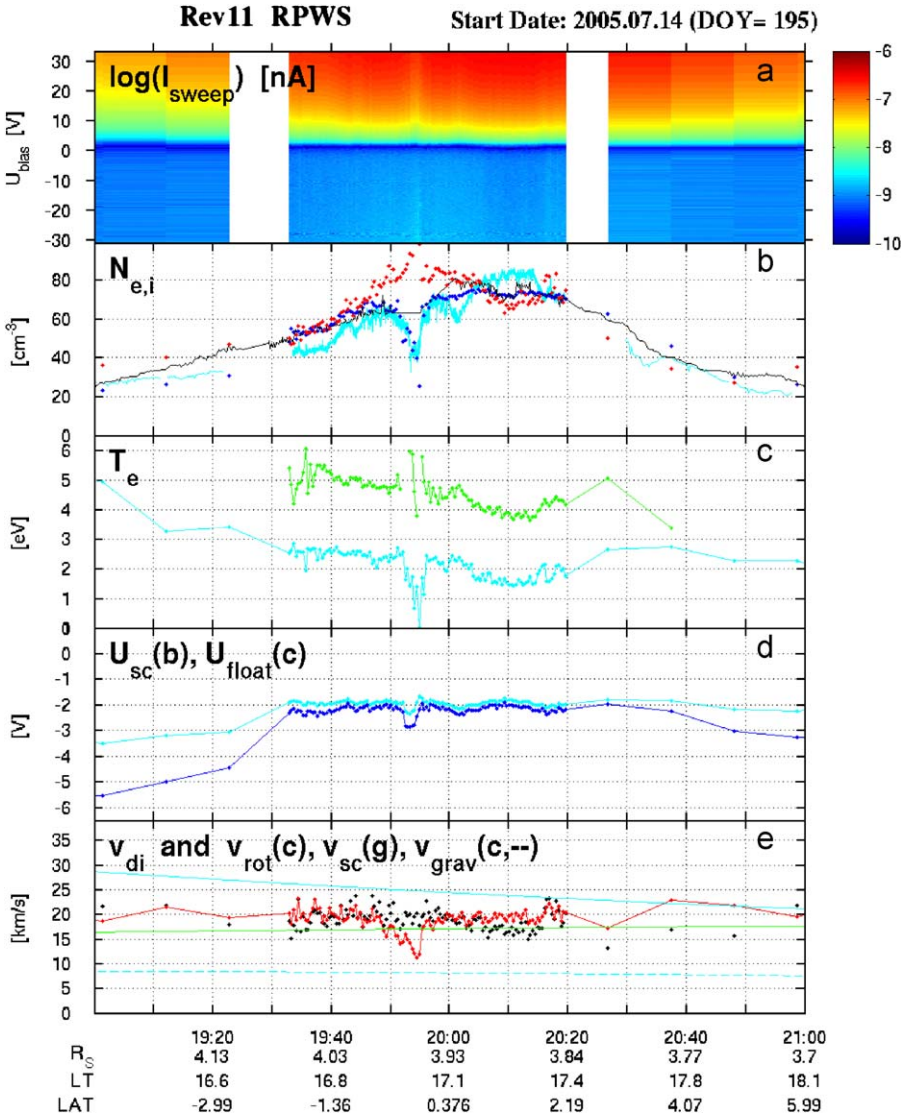

Fig. 10. Same as in Fig. 8. Data were taken during the Enceladus E02 encounter. Note the difference in ion (red) and electron (blue & black & cyan) densities (panel b). Average ion drift speeds (red & black) are again below the nominal co-rotation speed (cyan, panel e).

the time interval 19:45–20:05 UT, the ion density is significantly larger than the electron density. This is often observed during other ring plane crossings near Enceladus orbit (see also Farrell et al., 2009; Yaroshenko et al., 2009). The $n_e \neq n_i$ region corresponds rather well with the region of enhanced dust levels as detected by the long RPWS antenna (Fig. 11), as well as the dust counter experiment (CDA; S. Kempf, private communication). The assumptions behind the derived ion density are

- The average ion mass is close to 18 amu.
- The ion random flux is not affected by large fluxes of secondary electrons from energetic particles or dust impacts.
- The photoelectron current has been accurately compensated for.

We are certain that the first and third assumptions are valid, while secondary electrons from dust impacts on the LP sensor (or a direct charged dust current to the LP sensor) is more difficult to account for. However, the derived ion drift speeds from the measured ion random flux (black, panel e, Fig. 10) compare very well with those derived from the ion current gradient (red), which indicate that the secondary electrons levels cannot be very large during this particular event. The difference, $\Delta n = (n_i\text{-}n_e) \approx 40\text{–}60$ cm^{-3}, between the number densities of free electrons and ions are also in agreement with model calculations of charging levels and dust distributions during this and other events (Yaroshenko et al., 2009). We can here make an order-of-magnitude estimate of the mean charge levels of dust particles. Larger μm-sized particles should have charging levels close to 1500–2000 e C according to the estimated spacecraft potential for the event. Considering that smaller grains down to 10–100 nm can only carry a fraction of this charge, the total charged dust number densities for this event should be of the order 0.01–0.1 cm^{-3} when using a $r_d^{-\mu}$ size distribution of dust with $\mu \approx 4\text{–}5$ (e.g., Kempf et al., 2008). Further corrections to this order-of-magnitude estimate may occur, since it does not, for instance, take into account a possible enhancement of emitted secondary electrons from small grains (Chow et al., 1993; and references therein).

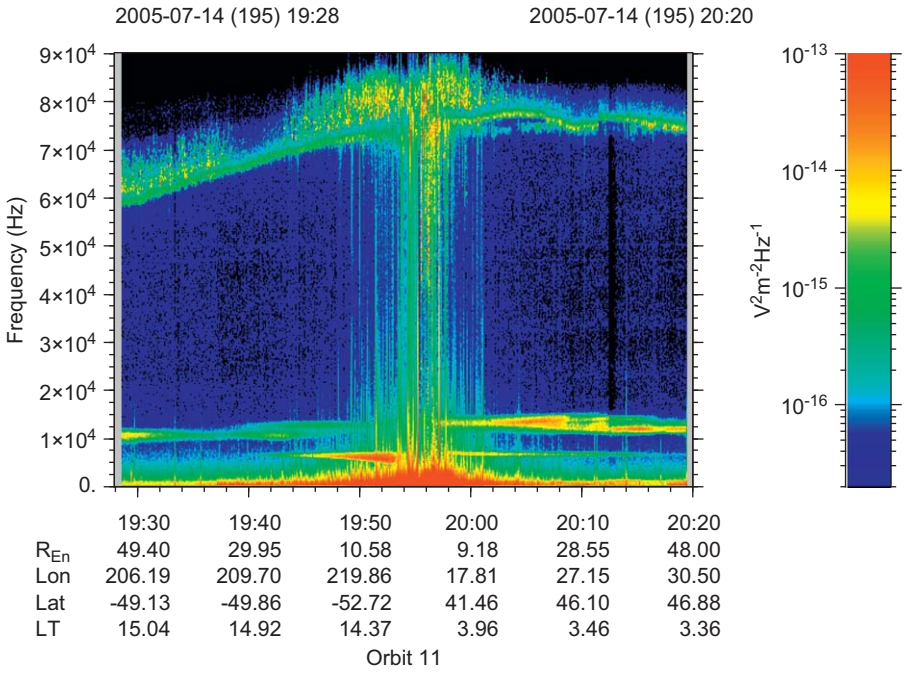

Fig. 11. RPWS emissions during the Enceladus E02 encounter. The upper hybrid line is difficult to identify near closest approach, because of the broadband noise generated by the intense fluxes of dust that hits the long antenna. The region of enhanced dust exists between 19:40 and 20:10 UT, which corresponds well with the period when the Langmuir probe detects a difference between the electron and ion number densities (see Fig. 10).

6. Discussion

6.1. Nature of measured density inhomogeneities

The measured density inhomogeneities ($\delta n/n$) by the interferometer experiment revealed two frequency regions with different phase response characteristics, one region below 200 Hz that was consistent with a co-rotating plasma, and one region in the 200–400 Hz interval that was consistent with a plasma close to the spacecraft speed ($\pm$a few km/s), i.e., consistent with a near Keplerian (gravitational) speed around Saturn. At these low frequencies the inhomogeneities have to be connected to the ion dynamics and therefore could follow (or be close to) the ion acoustic dispersion for water group ions (see e.g., Wahlund et al., 1998). In the one-dimensional case for one ion species-electron plasma (assuming isotropic Maxwellian distributions, small amplitude waves, $v_{\mathrm{th,i}} \ll |\omega/k| \ll v_{\mathrm{th,e}}$, and $\omega_{\mathrm{pi}} \gg \Omega_{\mathrm{i}}$), the ion acoustic dispersion looks like

$$\omega = \frac{k\omega_{\mathrm{pi}}}{k_{\mathrm{De}}(1+k^2/k_{\mathrm{De}}^2)1/2}\left[\frac{1}{2}+\frac{1}{2}(1+\beta)^{1/2}\right]^{1/2}$$

where

$$\beta = 12\frac{T_{\mathrm{i}}}{T_{\mathrm{e}}}\left(1+\frac{k^2}{k_{\mathrm{De}}^2}\right)$$

We have plotted this dispersion for a $T_{\mathrm{e}}/T_{\mathrm{i}} = 2$, $T_{\mathrm{e}} = 4$ eV, and $n_{\mathrm{e}} = 70\,\mathrm{cm}^{-3}$ plasma in Fig. 12. Scale sizes (wavelengths) for a water group dominated plasma in the frequency range 200–450 Hz would be between λ_{D} and 4.5 m, while those below 200 Hz would have larger scale sizes (wavelength). It is important, though, that the observed inhomogeneities (fluctuations) can be interpreted as spatial structures in the ion plasma instead of propagating ion acoustic waves (which require $T_{\mathrm{e}} > T_{\mathrm{i}}$) or possibly dust-ion acoustic waves (Shukla and Silin, 1992). However, the data do not mutually exclude one or the other explanation. The interferometer data (assuming spatial structures) would be consistent with scale sizes ($s_{\mathrm{inhom}} = v_{\mathrm{inhom}} \cos\theta_{\mathrm{sd}}/f$) of at most a few meters for the slow 200–400 Hz data, while the fast co-rotating inhomogeneities below 200 Hz are consistent with scale sizes larger than 100 m. The slow Keplerian inhomogeneities are therefore of the same order or smaller than the plasma Debye length. We interpret the slow inhomogeneities as associated with charged dust drifting close to the gravitational speed around Saturn, and could be related to, e.g., dust wakes generated by the charged dust in a drifting plasma (Winske et al.,

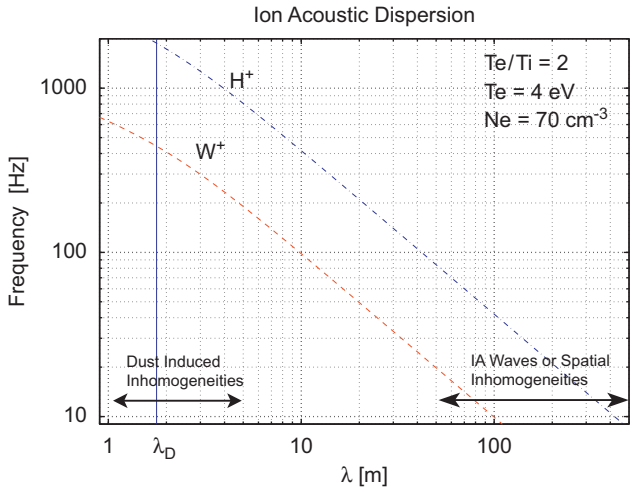

Fig. 12. Ion-acoustic dispersion relation for water group ions (red, W^+) and hydrogen ions (blue, H^+) corresponding to the event during Rev17. The Debye length was close to 2 m. The sizes of the measured inhomogeneities are noted in the figure assuming they are spatial. The Keplerian population corresponds to spatial scales near the Debye length, while the co-rotation populations have longer scale lengths/wavelengths. See text for further description.

2000). The faster inhomogeneities can be regarded as spatial inhomogeneities or (dust-) ion acoustic waves following the co-rotation of Saturn.

6.2. Ion temperature

The observed ion drift speeds (10–20 km/s) can be used to put an upper limit on the ion temperatures (T_i), since the ion random current is more fully written as

$$I_{i0} \approx -A_{LP} n_i q_i \sqrt{\frac{v_i^2}{16} + \frac{eT_i[eV]}{2\pi m_i}}$$

If the whole ion random current, except a gravitational speed contribution of 5 km/s, was due to the thermal contribution (the second term on the right-hand side), this would require $T_i < 1$–8 eV. The dominant (average) ion population at distances of 4–5 R_S is therefore inferred to be rather cold and the presented LP derived ion drift speeds must be regarded as over-estimations.

6.3. A dusty plasma

The Debye lengths vary between 1 and 5 m during the presented events. Dust number densities are certainly larger than those 0.1 m^{-3} measured by RPWS and CDA (for >1 μm-sized dust, e.g., Kempf et al., 2008), considering the steep power law dust size distributions detected. In the case of the presented Enceladus E02 event, dust densities may even reach 0.01 cm^{-3}. The situation in the near equatorial plasma disk surrounding the E-ring is therefore such that several charged dust particles exist within a Debye cube, which can then be called a collective dust-plasma ensemble. Newly created ions from e.g., photo-ionization would initially have a small energy, consistent with <1–8 eV estimations presented here, before being picked-up by the co-rotational electric field. The gyro-radius of water group ions in the presented events vary between 500 and 2000 m, which means that newly created water group ions may collectively interact (or collide electro-statically) with charged dust before completing a gyro-motion. The low energy ions can become scattered or trapped in the potential wells of the charged dust particles (since $|U_{SC}| \geqslant T_i$, and $U_{SC}/\lambda_D \sim 1$ V/m $\gg E_{rot} \sim 0.01$ V/m), and gyro-motion pick-up by a co-rotational electric field will therefore be severely inhibited (Fig. 13). The $\delta n/n$ interferometer results presented here also clearly show two distinct populations, not a smooth transition from lower to higher speeds that would be expected from collisions alone. The charged dust particles themselves are massive and are dominated by the gravitational force from Saturn. Likewise, the electron motion will be affected (repelled) by the negatively charged dust particles since $|U_{SC}| \geqslant T_e$ and $r_{ge} \approx 3$–10 m. Eventually, the co-rotation electric field will accelerate some ions to co-rotation speed, which then become energised and not very much affected by the negative dust potentials since $|U_{SC}| < T_{i,corot}$.

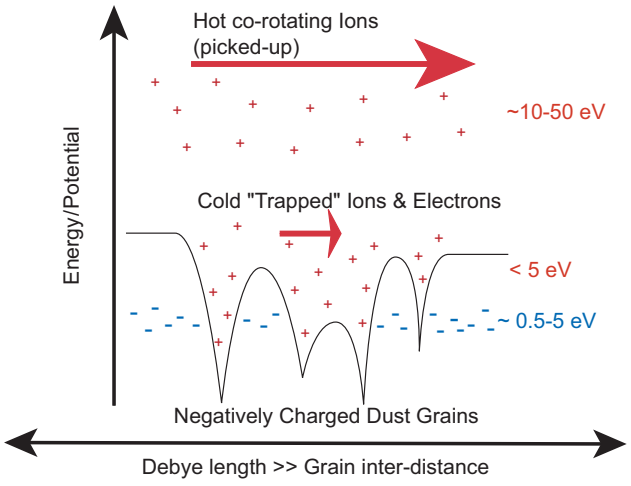

Fig. 13. Cartoon describing the physical picture as interpreted from the RPWS measurements. Ionized electron-ion pairs start with low energies, become trapped to a large degree by the steep potential gradients near the charged dust grains. Eventually, part of the ion population becomes accelerated by the co-rotation electric field around Saturn, and attain the larger co-rotation energies and can move more freely through the dusty plasma.

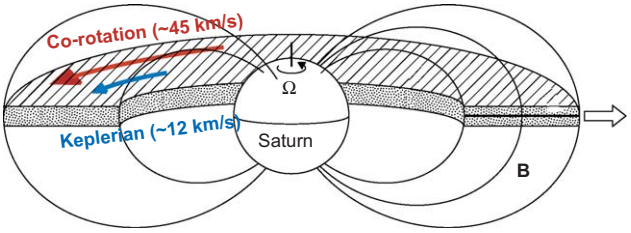

Fig. 14. Results presented here give observational evidence for that two ion populations with different drift speeds rotate around Saturn in the dusty plasma disk surrounding the E-ring. This may give rise to a current system that connects to Saturn's polar ionospheric regions, and possibly contribute to the release of plasma near the plasma disk edge near 8 R_S under the action of the centrifugal force.

The concluding cartoons of the physical situation that can explain all the RPWS observations presented here are displayed in Figs. 13 and 14. Fig. 14 shows the E-ring plasma disk region of negatively charged dust particles. The LP derived spacecraft potentials become positive outside 6–8 R_S, and the dust population is expected to lose its trapped ions at this distance from Saturn. A plasma disk outflow to the outer magnetosphere by the centrifugal force would therefore arise and is observed (e.g., Persoon et al., 2005; Morooka et al., 2009).

7. Conclusions

We have presented Cassini RPWS observations that reveal collective dust-plasma interactions such that $r_d \ll d_g \ll \lambda_D$ within the plasma disk close to the E-ring of Saturn. The negatively charged dust number densities at times even becomes large enough to cause $n_i > n_e$ (the number density of free electrons). Two different types of ion populations with associated $\delta n/n$ characteristics (inhomogeneities) are detected. One is co-moving with negatively charged dust particles near Keplerian speed around Saturn, and the other has been picked-up and energised above the dust potentials by the co-rotation electric field and move with the co-rotation speed around Saturn. This would be expected to generate current systems that flow azimuthally in the plasma disk and connect to the polar ionosphere of Saturn, and would also be expected to contribute to the generation of a centrifugally driven outflow of plasma to the magnetosphere outside about 6–8 R_S, where the dust potentials become positive.

Acknowledgements

The Swedish National Space Board (SNSB) supports the RPWS/LP instrument on board Cassini. The authors also thank for useful discussions with Rolf Boström and Nils Brenning.

References

Alfvén, H., 1984. The plasma universe. Space Sci. Rev. 39, 65.

Bonnell, J., Kintner, P.M., Wahlund, J.-E., Lynch, K., Arnoldy, R., 1996. Interferometric determination of broadband ELF wave phase velocity within a region of transverse auroral ion acceleration. Geophys. Res. Lett. 23, 3297.

Chow, V.W., Mendis, D.A., Rosenberg, M., 1993. Role of grain size and particle velocity distribution in secondary electron emission in space plasmas. J. Geophys. Res. 98, 19065.

Dessler, A.J., Sandel, R.R., Atreya, S.K., 1981. Planet. Space Sci. 29, 215.

Eriksson, A.I., Boström, R. 1995. Measurements of plasma density fluctuations and electric wave fields using spherical electrostatic probes. IRF Scientific Report, 220.

Eriksson, A.I., Wahlund, J.-E., 2006. Charging of the Freja satellite in the auroral zone. IEEE Trans. Plasma Sci. 34, 2038.

Fahleson, U., Fälthammar, C.-G., Pedersen, A., 1974. Ionospheric temperature and density measurements by means of spherical double probes. Planet. Space Sci. 22, 41.

Farrell, W.M., Kurth, W.S., Gurnett, D.A., Johnson, R.E., Kaiser, M.L., Wahlund, J.-E., Waite Jr., J.H., 2009. Plasma waves in the context of water-gas and water-ice in the near-vicinity of Enceladus. Geophys. Res. Lett., in press.

Goertz, C.K., 1989. Dusty plasmas in the solar system. Rev. Geophys. 27, 2.

Goertz, C.K., Morfill, G.E., Ip, W.-H., Grün, E., Havnes, O., 1986. Electromagnetic angular momentum transport in Saturn's rings. Nature 320, 141.

Grard, R.J., 1973. Properties of the satellite photoelectron sheath derived from photoemission laboratory measurements. J. Geophys. Res. 78, 2885.

Gurnett, D.A., et al., 2004. The radio and plasma wave science investigation. Space Sci. Rev. 114, 395.

Gurnett, D.A., Persoon, A.M., Kurth, W.S., Groene, J.B., Averkamp, T.F., Dougherty, M.K., Southwood, D.J., 2007. The variable rotation period of the inner region of Saturn's plasma disk. Science 316, 442.

Gustafsson, G., Wahlund, J.-E., 2009. Electron temperatures in Saturn's plasma disk, Planet. Space Sci., in preparation.

Havnes, O., Næsheim, L.I., Hartquist, T.W., Morfill, G.E., Melandsø, F., Scheicher, B., Trøim, J., Blix, T., Thrane, E., 1996. Meter-scale variations of the charge carried by mesospheric dust. Planet. Space Sci. 44, 1191.

Hill, J.R., Mendis, D.A., 1982. The dynamical evolution of the Saturnian ring spokes. J. Geophys. Res. 87, 7413.

Hill, T.W., Dessler, A., Michel, F., 1974. Configuration of the Jovian magnetosphere. Geophys. Res. Lett. 1, 3.

Hill, T.W., Michel, F.C., 1976. Heavy-ions from Galilean satellites and centrifugal-distortion of Jovian magnetosphere. J. Geophys. Res. 81, 4561.

Holmgren, G., Kintner, P.M., 1990. Experimental evidence of widespread regions of small scale plasma irregularities in the magnetosphere. J. Geophys. Res. 95, 6015.

Horányi, M., 1996. Charged dust dynamics in the solar system. Annu. Rev. Astron. Astrophys. 34, 383.

Horányi, M., 2000. Dust streams from Jupiter and Saturn. Phys. Plasmas 7, 3847.

Horányi, M., Hartquist, T.W., Havnes, O., Mendis, D.A., Morfill, G.E., 2004. Dusty plasma effects in Saturn's magnetosphere. Rev. Geophys. 42, RG4002.

Horányi, M., Juhász, A., Morfill, G.E., 2008. Large-scale structure of Saturn's E-ring. Geophys. Res. Lett. 35.

Hoegy, W.R., Brace, L.H., 1999. Use of Langmuir probes in non-Maxwellian space plasmas. Rev. Sci. Inst. 70, 3015.

Jacobsen, K.S., Wahlund, J.-E., Pedersen, A., 2009. Cassini Langmuir probe measurements in the inner magnetosphere of Saturn. Planet. Space Sci. 57, 48–52.

Jones, G.H., Coates, A.J. Kanani, S. Arridge, C.S. Young, D. Crary, F. 2008. The structure of Enceladus's plume as observed by Cassini CAPS-ELS. Poster presented at Saturn symposium in London.

Kelley, M.C., Mozer, F.S., 1972. A technique for making dispersion relation measurements of electrostatic waves. J. Geophys. Res. 77, 6900.

Kellog, P.J., Goetz, K., Manson, S.J., 2009. Plasma wave measurements with STEREO-S/WAVES: calibration, potential model and preliminary results. J. Geophys. Res., 114, A02107, doi:10.1029/2008JA013566.

Kempf, S., Beckmann, U., Moragas-Klostermeyer, G., Postberg, F., Srama, R., Economou, T., Schmidt, J., Sphan, F., Grün, E., 2008. The E-ring in the vicinity of Enceladus I. Spatial distribution and properties of the ring particles. Icarus 193, 420.

Kempf, S., Beckmann, U., Srama, R., Horányi, M., Auer, S., Grün, E., 2006. The electrostatic potential of E ring particles. Planet. Space Sci. 54, 999.

Kempf, W.S., Srama, R., Postberg, F., Burton, M., Green, S.F., Helfert, S., Hillier, J.K., McBride, N., Anthony, J., McDonnell, M., Moragas-Klostermeyer, G., Roy, M., Grün, E., 2005. Composition of Saturnian stream particles. Science 307, 1274.

Kurth, W.S., Averkamp, T.F., Gurnett, D.A., Wang, Z., 2006. Cassini RPWS observations of dust in the Saturn's E ring. Planet. Space Sci. 54, 988.

Medicus, G., 1962. Spherical Langmuir probe in "drifting" and "accelerated" Maxwellian distribution. J. Appl. Phys. 33, 3094.

Moncuquet, M., et al., 2005. Quasi thermal noise spectroscopy in the inner magnetosphere of Saturn with Cassini/RPWS: electron temperatures and density. Geophys. Res. Lett. 32.

Morfill, G.E., Annaratone, B.M., Bryant, P., Ivlev, A.V., Thomas, H.M., Zuzic, M., Fortov, V.E., 2002. A review of liquid and crystalline plasma – new physical states of matter? Plasma Phys. Control. Fusion 44, 263.

Morooka, M.W., Modolo, R., Wahlund, J.-E., André, M., Eriksson, A.I., Persoon, A.M., Gurnett, D.A., Kurth, W.S., Coates, A.J., Lewis, G.R., Khurana, K.K., Dougherty, M., 2009. Ann. Geophys., accepted for publication.

Mott-Smith, H.M., Langmuir, I., 1926. The theory of collectors in gaseous discharges. Phys. Rev. 28, 727.

Northrop, T.G., 1992. Dusty plasmas. Phys. Scripta 45, 475.

Persoon, A.M., et al., 2005. Equatorial electron density measurements in Saturn's inner magnetosphere. Geophys. Res. Lett. 32, L23105.

Scmidt, J., Brilliantov, N., Spahn, F., Kempf, S., 2008. Slow dust in Enceladus' plume from condensation and wall collisions in tiger stripe fractures. Nature 451.

Shukla, P.K., Silin, V.P., 1992. Dust ion-acoustic wave. Phys. Scripta 45, 508.

Smith, B.A., et al., 1981. Encounter with Saturn: Voyager 1 imaging science results. Science 212, 163.

Srama, R., et al., 2006. In situ dust measurements in the inner Saturnian system. Planet. Space Sci. 54, 967.

Sittler Jr., E.C., Thomsen, M., Johnson, R.E., Hartle, R.E., Burger, M., Chornay, D., Shapiro, M.D., Simpson, D., Smith, H.T., Coates, A.J., Rymer, A.M., McComas, D.J., Young, D.T., Reisenfeld, D., Dougherty, M., Andre, N., 2006. Cassini observations of Saturn's inner plasmasphere: Saturn orbit insertion results. Planet. Space Sci. 54, 1197.

Temerin, M., 1978. The polarization, frequency, and wavelengths of high-latitude turbulence. J. Geophys. Res. 83, 2609.

Wahlund, J-E., Boström, R., Gustafsson, G., Gurnett, D.A., Kurth, W.S., Averkamp, T., Hospodarsky, G.B., Persoon, A.M., Canu, P., Pedersen, A., Desch, M.D., Eriksson, A.I., Gill, R., Morooka, M.W., André, M., 2005. The inner magnetosphere of Saturn: Cassini RPWS cold plasma results from the first encounter. Geophys. Res. Lett. 32.

Wahlund, J.-E., Eriksson, A.I., Holback, B., Boehm, M.H., Bonnell, J., Kintner, P.M., Seyler, C.E., Clemmons, J.H., Eliasson, L., Knudsen, D.J., Nordqvist, P., Zanetti, L.J., 1998. Broadband ELF plasma emission during auroral energization 1: slow ion acoustic waves. J. Geophys. Res. 103, 4343.

Whipple Jr., E.C., 1965. The equilibrium electric potential of a body in the upper atmosphere and in interplanetary space, PhD thesis.

Winske, D., Daughton, W., Lemons, D.S., Murillo, M.S., 2000. Ion kinetic effects on the wake potential behind a dust grain in a flowing plasma. Phys. Plsamas 7, 2320.

Yaroshenko, V.V., Ratynskaia, S., Olson, J., Brenning, N., Wahlund, J.-E., Morooka, M.W., Kurth, W.S., Gurnett, D.A., Morfill, G.E., 2009. Characteristics of charged dust inferred from the Cassini RPWS plasma measurements in the vicinity of Enceladus. Planet Space Sci., in press, doi:10.1016/j.pss.2009.03.002.

Young, D.T., et al., 2005. Composition and dynamics of plasma in Saturn's magnetosphere. Science 307, 1262.